ECS Transactions, 35 (1) 2097-2104 (2011)
10.1149/1.3570200 ©The Electrochemical Society

Strain Effects on the Surface Chemistry of $La_{0.7}Sr_{0.3}MnO_3$

Jeong Woo Han[a] , Helia Jalili[a], Yener Kuru[a,b], Zhuhua Cai[a], and Bilge Yildiz[a]

[a] Laboratory for Electrochemical Interfaces
[b] Department of Materials Science and Engineering
Massachusetts Institute of Technology, Cambridge, Massachusetts 02139, USA

We report on the mechanistic effects of epitaxial strain on the surface chemistry, in particular the segregation of Sr cations on $La_{0.7}Sr_{0.3}MnO_3$ (LSM) model dense thin films. Our results show that the LSM film surfaces are layered and exhibit strain-dependent nanoscale lateral structures. All surfaces examined here were Sr-rich. X-ray photoelectron spectroscopy shows a larger Sr segregation tendency for the tensile strained LSM films. This result is in good agreement with our first principles-based calculations, which predict lower Sr segregation energy on the tensile strained LSM surface. Our findings suggest the importance of lattice strain as a key parameter to tune the surface chemistry for facilitating oxygen reduction kinetics on transition metal perovskite cathode surfaces for solid oxide fuel cells.

Introduction

The relation of equilibrium surface segregation, that is the enhancement or depletion of a certain cations in the cathode at a given temperature and pressure, to oxygen reduction kinetics on solid oxide fuel cell (SOFC) cathodes is an outstanding question. In the perovskite structured $La_{1-x}Sr_xMnO_3$ (LSM), which is a widely used and studied SOFC cathode material, the ratio of A site to B site cations (A/B) can deviate from nominal stoichiometry significantly (1-6), due to an enrichment of Sr or La cations on the surface. In addition to the temperature and pressure as the thermodynamic and kinetic drivers, lattice mismatch between the substrate and cathode material can control the surface chemistry and electronic structure (7, 8).

Impact of the strain induced by substrate on the surface electronic structure and reactivity has been long demonstrated for low temperature noble metal electrocatalysts (8). On the other hand, the role of lattice strain on the surface chemistry, reactivity, and ionic conductivity of solid oxide fuel cell-related materials is attracting interest only recently. Examples include Kushima *et al.*'s work (7), which demonstrated that epitaxial strain directly influences oxygen-vacancy formation energy as well as oxygen adsorption energy on $LaCoO_3$, favoring both processes up to a critical strain. Sase *et al.* (9) have demonstrated that oxygen surface exchange coefficient at the hetero-interface of $La_{0.6}Sr_{0.4}CoO_3$ / $(La,Sr)_2CoO_4$ thin films is three orders of magnitude larger than that for the surface of single phase $La_{0.6}Sr_{0.4}CoO_3$ or $(La,Sr)_2CoO_4$ alone. A plausible hypothesis that can explain the enhanced oxygen exchange is the role of local strains at this interface. Garcia-Barriocanal *et al.* (10) reported an increase of eight orders of magnitude in ionic conductivity in 1-30 nm thick yttria stabilized zirconia layers that were coherently "strained" between dielectric $SrTiO_3$ layers. Although there have been controversy about

the ionic versus electronic nature of this enhancement in conductivity, this report intrigued interest in studying the strain effects also in the solid oxide fuel cell (SOFC) community. As a follow-up, Kushima *et al.* (11), using *ab initio* and atomistic computational methods, showed that epitaxial strain alone can indeed significantly increase the ionic conductivity, but not nearly as much as that reported by Garcia-Barriocanal *et al* (10).

In addition to the direct effects of strain on the oxygen sublattice of SOFC oxides, strain can also alter the surface structure and cation chemistry (1, 2, 6) – the focus of this paper. Surface cation segregation has an important role in controlling the reactivity of SOFC materials. In this paper we are reporting the theoretical and experimental studies of strain-induced changes in the surface segregation of cations on the $La_{0.7}Sr_{0.3}MnO_3$ films. The model systems that we employ are epitaxially strained LSM films deposited onto $SrTiO_3$ (STO) and $LaAlO_3$ (LAO) single crystal substrates, which induce tensile and compressive strains on LSM, respectively. Our analysis integrates surface sensitive characterization methods and first principles-based simulations, to assess the chemical environment on the LSM surface, in particular the segregation of Sr cations as a function of strain; experimentally probed with angle resolved X-ray Photoelectron Spectroscopy and computationally assessed through segregation energy calculations.

Methods

Experiment

Epitaxial LSM films were grown on (001) SrTiO3 (STO) and (001) $LaAlO_3$ (LAO) using pulsed laser deposition (12). X-ray diffraction (XRD) measurements were performed employing a PANalytical Expert Pro MPD diffractometer. 2θ-ω scans were carried out to investigate the phase purity and orientation. Scanning tunneling microscopy/spectroscopy (STM/STS) at room temperature (RT) was performed to identify the surface and electronic structure of strained films. Chemical composition and cation valance states were identified using angle resolved X-ray photoelectron spectroscopy (XPS). These surface sensitive measurements were performed in a modified ultrahigh vacuum (UHV) system, designed by Omicron Nanotechnology, Inc, with base pressure better than 5×10^{-10} Torr. The analysis chamber was equipped with a five-channel hemispherical electron analyzer and an x-ray source for the XPS. The as-grown films were cleaned in ultrasonic bath with 99.99% purity ethyl-alcohol, followed by Ar blow drying. In order to remove carbon contamination prior to the STM/STS measurements, sample surfaces were cleaned by heating in oxygen pressure of 5×10^{-5} mbar at 500°C for 30 min in the UHV chamber. A pyrolytic Boron Nitride (PBN) heater was used to evenly heat the LSM films during the cleaning process. Monitoring the change in carbon peak revealed that this annealing process can reduce the carbon contamination down to 1-3%. STM was performed in the constant-current mode using etched Pt/Ir tips. 1-2V of bias voltage and 200-500 pA of tunneling feedback current were used during the STM imaging.

Computation

The surface segregation energy, which is the energy required for moving an impurity from the inside of a host metal to the surface (13, 14), is a key parameter in determining

which component prefers to enrich on the surface the material. First-principles calculations have proven to be useful in determining surface segregation thermodynamics not only for transition metals (14, 15) but also for transition metal oxides (16). We therefore assess the surface segregation energy of Sr as a measure of the role of strain to induce an enrichment or depletion of Sr on the A-site on LSM surface. We performed plane wave DFT calculations using the Vienna *ab initio* simulation package (VASP) (17, 18) to assess surface segregation energetics of Sr on the LSM surface under a range of strains, from -3.5% (compressive) to +2% (tensile), including -3% and +1% that correspond to the ones induced by LAO and STO in LSM, respectively. We employed the generalized gradient approximation (GGA) parameterized by Perdew and Wang (19) along with the projector augmented wave (PAW) method (20, 21) to describe ionic cores. To avoid the self-interaction errors that occur in the traditional DFT for strongly correlated electronic systems, we employed the DFT+*U* method accounting for the on-site Coulomb interaction in the localized *d* or *f* orbitals. The correction parameter of effective U-J = 4 eV was chosen, as previously determined by Wang *et al.* (22) through fitting the enthalpies of oxidation reactions. All calculations used a plane wave expansion cutoff of 400 eV and included spin polarization. Geometries were relaxed using a conjugate gradient algorithm until the forces on all unconstrained atoms were less than 0.03 eV/Å.

The DFT-optimized cubic lattice constant of LSM was 3.93 Å, in good agreement with the experimental value of 3.88 Å. 2D-planar lattice strain was then imposed by elongating the simulation cell in the *x* and *y* directions and relaxing the cell configuration and dimension in the *z* direction. This bulk structure of $LaMnO_3$ was cleaved along the (001) plane to construct a surface consistent with our PLD-grown epitaxial films. The slab model is 15.5 Å thick and contains 9 atomic symmetric layers with the middle 3 layers constrained in their bulk positions. The symmetric slab was chosen to avoid the fictitious dipole moment (23). We have focused only on the (001) La-terminated surface to model the substitution of Sr atom with La atom on the surface. For all calculations, a vacuum spacing of 15 Å was placed in the direction of surface normal. We have chosen a (2×2) surface unit cell and a 4×4×1 Monkhorst-Pack *k*-point mesh which was sufficient to give well converged results.

To compare the strain-free concentration effects on the segregation, we have constructed two models, one with 25% (X_s=1/4) and another one 50% (X_s=1/2) Sr on A site on the surface. Surface segregation energy was calculated using Eq. [1].

$$E_{seg} = \frac{1}{2}\left\{\frac{1}{2}\left(E_{surf}\left(2x\right) + E_{surf}\left(0\right)\right) - E_{bulk}\left(x\right)\right\}, \qquad [1]$$

where E_{seg} is surface segregation energy per a Sr atom, E_{surf} the total energy of a slab with Sr atoms occupying La sites on a surface (i.e. top and bottom layer of the slab), E_{bulk} the total energy of a slab with Sr atoms occupying La sites in the bulk (i.e. central layer of the slab), *x* the number of Sr atoms in the unit cell (16, 24, 25). Figure 1 schematically shows our model. For X_s=1/2, we put two Sr atoms into each top and bottom layer in the unit cell, while for X_s=1/4, we put one Sr atom into each top and bottom layer while remaining two Sr atoms in the central layer of the slab. The latter corresponds closely to our experimental observation in which Sr fraction on the surface (in bulk nominal) ~40% (30%). For both our models, Sr fraction on the total A sites is 20%.

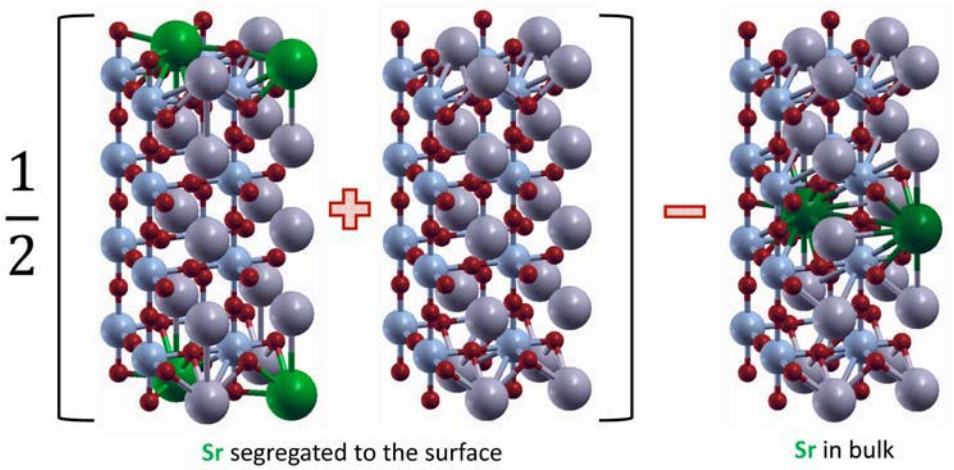

Figure 1. The model used to calculate the segregation energy per Sr atom when X_s=1/2. For X_s=1/4, we substituted only one Sr atom on top and bottom surfaces and two Sr atoms in the middle layer (not shown here). La atoms are gray spheres, Sr atoms are green spheres, Mn atoms are light blue spheres, O atoms are red spheres.

Results and Discussion

XRD, 2θ-ω scans were performed for the bare substrates of STO and LAO as well as LSM films grown on STO and LAO. Comparison of the 2θ-ω scans of the films with the ones obtained for the bare substrates revealed that LSM thin films are single phase and their c-axes are oriented perpendicular to the film surface. XRD results (not shown here) indicate that both layers are fully strained; the film on STO has approximately 1% in-plane tensile strain whereas the one on LAO is under -3% in-plane compression, with (001) out of plane orientations.

Figure 2 shows the STM images of the cleaned surface of LSM/LAO (a) and LSM/STO (b) at room temperature. LSM surface grown on both substrates (LAO and STO) is atomically smooth with the average roughness less than 0.1 nm. Well resolved

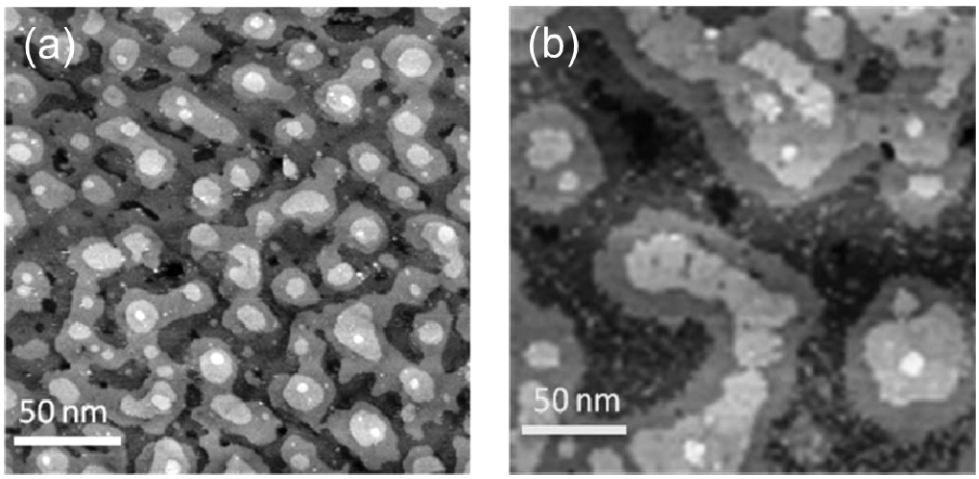

Figure 2. Surface morphology of the 10 nm thick (a) LSM/LAO, and (b) LSM/STO films at room temperature. STM images were taken with tunneling feedback current of 0.2 nA, and bias voltage of 2 V.

terraces with different sizes can be clearly seen on both substrates. The height profiles (not shown) of these terraces show that the height difference between each layer is 4.0±0.3 Å which is in good agreement with the lattice parameter of the LSM (3.88 Å). The overall morphology on these two substrates is similar. While growth of large terraces atop with smaller islands is evident on both substrates, the size of these islands on LSM/LAO is significantly smaller.

The La 4*d* and Sr 3*d* peaks were used for assessing the relative presence of Sr on the A-site and the Sr chemical environment on the surface. Since La 4*d* and Sr 3*d* emissions have similar kinetic energies, the probed depth (~3 nm) is nearly identical for both emissions (1). Figure 3(a) shows the ratio of the integral intensity for Sr 3*d* and La 4*d*, calculated from the XPS data (shown in Figure 3b) for LSM/STO (black bars), LSM/LAO (red bars). These spectra were measured at two different angles, 0° and 70°, between the surface normal and detector position. Analyzing the XPS spectra at 70° emissions with a probing depth of ~1 nm (26) gives more information about the surface compared to the normal angle (0°) emission with a probing depth of ~3 nm. As shown in Figure 3(a), for both samples of LSM/LAO and LSM/STO, the total Sr/(La+Sr) is larger than the nominal value of 0.3, suggesting Sr enrichment on the surface. Note that the difference between the total Sr/(La+Sr) obtained at θ=0° and θ=70° is within the error bars of our measurement and fitting analysis. A-site enrichment of LSM has been addressed by many groups and different mechanisms were proposed for its origin. Bertacco *et al* (1) used angle resolved XPS (θ=0-70°) and observed a 20% increase of Sr/La ratio by changing the angle from 0° to 70° on LSM grown on STO. Quantification was done using the Sr 3*d* and La 4*d* peaks. Dulli *et al* (27), on the other hand, observed as high as 50% increase of Sr over La, using the Sr 3*d* and La 3*d* peaks, for LSM grown on LAO. This increase was explained based on the restructuring the surface to form a Ruddlesden-Popper phase on the surface. The enhancement of Sr on the LSM surface on LAO or STO in the present investigation is not as high as those reported by Bertacco *et al* (1) and Dulli *et al* (27). Moreover, as shown in the STM images in Figure 2, the height difference between each surface layer is consistent with the lattice parameter of LSM and no evidence of existence of Ruddlesden-Popper phase or SrO phases was noted on our LSM surfaces.

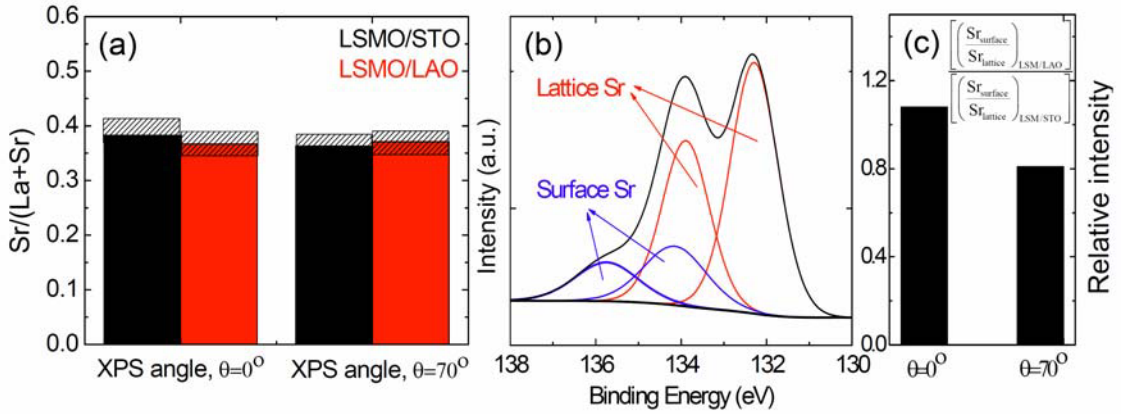

Figure 3. (a) Integral intensity of Sr/(La+Sr) obtained for LSM/STO (black bars) and LSM/LAO (red bars). (b) Sr 3*d* region in the photoelectron spectra for the cleaned surface of LSM/LAO. (c) Ratio of integral intensity of the Sr main peaks (red curve in b) to the Sr shoulder peaks (blue curve in b) of LSM/LAO over LSM/STO.

To obtain more quantitative information about the formation of secondary phases or differences in the chemical state on LSM surfaces as a function of strain, we analyzed the Sr 3*d* spectra by curve fitting (Figure 3b). The Sr *3d* core level consists of two major components, which we assign to arise from the perovskite lattice (main peak) and from surface species (secondary peak). Position of the main peak of Sr 3*d* at the lower binding energy is at 132±0.2 eV. This peak is attributed to Sr bound within the perovskite structure. The secondary peak arises from (non-perovskite) surface contribution, likely SrO-related species, and is at 133.4 ± 0.2 eV (1, 28, 29) Note that the secondary peak has higher binding energy compared to the main lattice peak. Higher binding energy shoulder is evident in O1*s* (not shown) but it is more subtle in Sr 3*d*. The ratio between the main peak of Sr to the Sr surface component at the higher binding energy can serve as a measure of surface segregation tendency of Sr on LSM. Thus, we quantified this ratio (Figure 3c) for the tensile strained LSM film on STO ($(Sr_{surface}/Sr_{lattice})_{LSM/STO}$) and for the compressive strained LSM film on LAO ($(Sr_{surface}/Sr_{lattice})_{LSM/LAO}$) to compare the Sr segregation tendency as a function of LSM strain. The ratio $[(Sr_{surface}/Sr_{lattice})_{LSM/LAO}]/[(Sr_{surface}/Sr_{lattice})_{LSM/STO}]$ changes from 1.08±0.05 for 0° emission to 0.8±0.04 for 70° emission. This result shows that Sr segregates to the surface of LSM/STO more than on LSM/LAO, suggesting that tensile strain induces more Sr on the surface of LSM.

We interpret the above result in light of DFT calculations of segregation energy of Sr, E_{seg}, as a function of strain. By definition, negative E_{seg} favors Sr on the surface compared to in the bulk. From the results shown in Figure 4, we first note that the Sr favors to segregate to the surface regardless of the amount and sign of strain from -3.5% to +2%, consistent with the previous experimental and theoretical reports (16, 30). If an element's atomic size is larger and/or its cohesive energy is less than that of the other, it would be more easily segregated to the surface (31). Here, the ionic radius of Sr (1.12 Å) is larger than that of La (1.06 Å) and the surface tension of Sr (0.29 J/m^2) that is representative of its cohesive energy is less than that of La (0.74 J/m^2) (32). Fister *et al.* suggested that reducing the polarity of the (La, Sr)O planes at the surface may be another driving force for Sr segregation (5). More importantly, we predict that Sr segregation tendency increases as the strain increases from the compressive (-3.5%) to the tensile

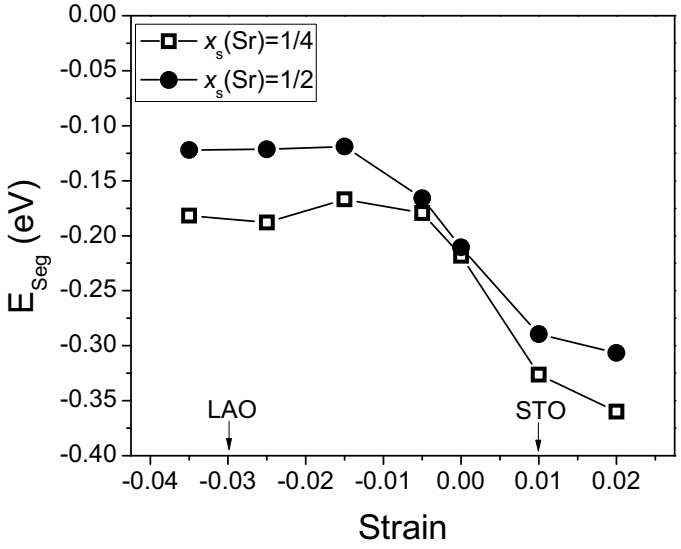

Figure 4. Surface segregation energies of Sr calculated from the LSM models using X_s=1/4 and X_s=1/2 under different strain states.

(2%). Our experimental and theoretical results are qualitatively in good agreement and clearly show that the tensile strain facilitates Sr segregation to the surface of LSM while the compressive strain suppresses this behavior.

Conclusion

Combining DFT calculations with high resolution surface sensitive techniques (STM and XPS), we investigated the effect of substrate-induced epitaxial strain on the surface chemical state, in particular Sr segregation on $La_{0.7}Sr_{0.3}MnO_3$. Both surfaces examined here were Sr-rich, with a larger tendency for Sr segregation for the tensile strained LSM. Our experimental and theoretical results are qualitatively in good agreement. These initial results indicate the importance of lattice strain as an important parameter to control the surface chemistry for oxygen reduction kinetics on SOFC's cathode.

Acknowledgments

We thank Prof. Paul Salvador's group at Carnegie Mellon University for providing the LSM samples. We acknowledge the US–DOE, Office of Fossil Energy, Grant No. DE–NT0004117 and Basic Energy Sciences, Grant No. DE-SC0002633 for financial support, and the National Science Foundation for computational support through the TeraGrid Advanced Support Program, Grant No. TG–ASC090058.

References

1. R. Bertacco, J. P. Contour, A. Barthélemy and J. Olivier, *Surf. Sci*. **511** (1-3), 366-372 (2002).
2. H. Kumigashira, K. Horiba, H. Ohguchi, K. Ono, M. Oshima, N. Nakagawa, M. Lippmaa, M. Kawasaki and H. Koinuma, *Appl. Phys. Lett.* **82** (20), 3430-3432 (2003).
3. M. P. de Jong, V. A. Dediu, C. Taliani and W. R. Salaneck, *J. Appl. Phys.* **94** (11), 7292-7296 (2003).
4. Q.-H. Wu, M. Liu and W. Jaegermann, *Mater. Lett*. **59** (16), 1980-1983 (2005).
5. T. T. Fister, D. D. Fong, J. A. Eastman, P. M. Baldo, M. J. Highland, P. H. Fuoss, K. R. Balasubramaniam, J. C. Meador and P. A. Salvador, *Appl. Phys. Lett.* **93** (15), 151904-151903 (2008).
6. K. Katsiev, B. Yildiz, K. Balasubramaniam and P. A. Salvador, *Appl. Phys. Lett.* **95** (9), 092106-092103 (2009).
7. A. Kushima, S. Yip and B. Yildiz, *Phys. Rev. B* **82** (11), 115435 (2010).
8. M. Mavrikakis, B. Hammer and J. K. Nørskov, *Phys. Rev. Lett.* **81** (13), 2819 (1998).
9. M. Sase, K. Yashiro, K. Sato, J. Mizusaki, T. Kawada, N. Sakai, K. Yamaji, T. Horita and H. Yokokawa, *Solid State Ionics* **178** (35-36), 1843-1852 (2008).
10. J. Garcia-Barriocanal, A. Rivera-Calzada, M. Varela, Z. Sefrioui, E. Iborra, C. Leon, S. J. Pennycook and J. Santamaria, *Science* **321** (5889), 676-680 (2008).
11. A. Kushima and B. Yildiz, *J. Mater. Chem.* **20** (23), 4809-4819 (2010).

12. K. R. Balasubramaniam, S. Havelia, P. A. Salvador, H. Zheng and J. F. Mitchell, *Appl. Phys. Lett.* **91** (23), 232901-232903 (2007).
13. A. V. Ruban and H. L. Skriver, *Comput. Mater. Sci.* **15** (2), 119-143 (1999).
14. A. V. Ruban, H. L. Skriver and J. K. Nørskov, *Phys. Rev. B* **59** (24), 15990 (1999).
15. A. U. Nilekar, A. V. Ruban and M. Mavrikakis, *Surf. Sci.* **603** (1), 91-96 (2009).
16. S. Piskunov, E. Heifets, T. Jacob, E. A. Kotomin, D. E. Ellis and E. Spohr, *Phys. Rev. B* **78** (12), 121406 (2008).
17. G. Kresse and J. Furthmuller, *Phys. Rev. B* **54** (16), 11169-11186 (1996).
18. G. Kresse and J. Hafner, *Phys. Rev. B* **47** (1), 558-561 (1993).
19. J. P. Perdew, J. A. Chevary, S. H. Vosko, K. A. Jackson, M. R. Pederson, D. J. Singh and C. Fiolhais, *Phys. Rev. B* **46** (11), 6671 (1992).
20. P. E. Blöchl, *Phys. Rev. B* **50** (24), 17953 (1994).
21. G. Kresse and D. Joubert, *Phys. Rev. B* **59** (3), 1758-1775 (1999).
22. L. Wang, T. Maxisch and G. Ceder, *Phys. Rev. B* **73** (19), 195107 (2006).
23. E. A. Kotomin, Y. A. Mastrikov, E. Heifets and J. Maier, *Phys. Chem. Chem. Phys*. **10** (31), 4644-4649 (2008).
24. A. Saul and M. Weissmann, *Phys. Rev. B* **60** (7), 4982 (1999).
25. C. Jiang and B. Gleeson, *Acta Mater*. **55** (5), 1641-1647 (2007).
26. http://www.nist.gov/srd/nist82.cfm.
27. H. Dulli, P. A. Dowben, S. H. Liou and E. W. Plummer, *Phys. Rev. B* **62** (22), R14629 (2000).
28. P. A. W. van der Heide, *Surf. Interface Anal*. **33** (5), 414-425 (2002).
29. G. Vovk, X. Chen and C. A. Mims, *J. Phys. Chem. B* **109** (6), 2445-2454 (2004).
30. R. Herger, P. R. Willmott, C. M. Schlepütz, M. Björck, S. A. Pauli, D. Martoccia, B. D. Patterson, D. Kumah, R. Clarke, Y. Yacoby and M. Döbeli, *Phys. Rev. B* **77** (8), 085401 (2008).
31. J. W. Han, J. R. Kitchin and D. S. Sholl, *J. Chem. Phys.* **130** (12), 124710-124718 (2009).
32. H. M. Lu and Q. Jiang, *J. Phys. Chem. B* **109** (32), 15463-15468 (2005).